PHYSICAL REVIEW B **98**, 134438 (2018)

Editors' Suggestion

Magnetic structure and spin correlations in magnetoelectric honeycomb $Mn_4Ta_2O_9$

N. Narayanan,[1,2,*] A. Senyshyn,[3] D. Mikhailova,[4] T. Faske,[5] T. Lu,[1] Z. Liu,[1] B. Weise,[4] H. Ehrenberg,[6] R. A. Mole,[2]
W. D. Hutchison,[7] H. Fuess,[5] G. J. McIntyre,[2] Y. Liu,[1,†] and D. Yu[2,‡]
[1]*Research School of Chemistry, The Australian National University, ACT 2601, Australia*
[2]*Australian Neutron Science and Technology Organisation, New Illawarra Road, Lucas Heights NSW 2234, Australia*
[3]*Heinz Maier-Leibnitz Zentrum (MLZ), Technische Universität München, Lichtenbergstrasse 1, 85748 Garching, Germany*
[4]*Leibniz Institute for Solid State and Materials Research (IFW) Dresden e.V., Helmholtzstrasse 20, D-01069 Dresden, Germany*
[5]*Structure Research Division, Institute for Materials Science, Darmstadt University of Technology,*
Alarich Weiss Strasse 2, 64287 Darmstadt, Germany
[6]*Institute for Applied Materials (IAM), Karlsruhe Institute of Technology (KIT), Hermann-von-Helmholtz-Platz 1,*
D-76344 Eggenstein-Leopoldshafen, Germany
[7]*School of PEMS, The University of New South Wales Canberra at ADFA, ACT 2600, Australia*

(Received 3 August 2018; revised manuscript received 18 September 2018; published 22 October 2018)

We elucidate the magnetic interactions and the role of spin (electron) correlation in determining the ground state of the honeycomb compound $Mn_4Ta_2O_9$, by neutron powder diffraction, inelastic neutron scattering (INS), specific-heat (C_P) measurements, and electronic-structure calculations. The antiferromagnetic long-range order with moments along c occurs at 102 K with strong exchange striction and small anisotropy. It is described by the three-dimensional Ising model. Diffuse magnetic scattering has been observed above T_N, which is attributed to the two-dimensional spin correlations within the Mn^{2+} honeycombs. This is confirmed by the calculated exchange constants. INS experiments and spin-wave simulations together with C_P measurements reveal two gapped modes on the ab plane, originating from the rotation of the spins away from the easy axis c. The magnetic anisotropy is mainly determined by an electron-correlation-assisted dipole-dipole interaction. This work provides insight into the competing origins of the magnetic anisotropy, which leads to different magnetic ground states in the family of honeycomb compounds.

DOI: 10.1103/PhysRevB.98.134438

I. INTRODUCTION

In magnetoelectric materials, magnetic ordering and electric polarization (EP) coexist where both magnetism and EP are of spin origin. In principle, the stronger the coupling of these two, the larger the magnetoelectric (ME) effect is expected. The magnetoelectric effect can be utilized in applications such as MRAMs, sensors, and capacitors. Although technically relevant, the coupling mechanism between these two orders is complicated [1–5]. Two classes of materials fulfill this requirement: (i) type-II multiferroics such as orthorhombic $RMnO_3$ ($R =$ rare earth) and $Ni_3V_2O_8$, where spontaneous EP is induced by the magnetic ordering (internal field) [6–9], and (ii) materials such as Cr_2O_3 and $LiMPO_4$ ($M =$ Co, Fe, Ni, Mn) which show no spontaneous EP in the ground state (GS) but an induced EP by the application of external magnetic field below the magnetic ordering temperature [3,10,11]. The above described magnetoelectrics and type-II multiferroics should be distinguished from the type-I multiferroics, in which magnetism and EP have different independent origins [4]. The magnetic order parameter should break both time-reversal and inversion symmetries [1].

In the present paper, we concentrate on the family of the honeycomb $M_4A_2O_9$ ($M =$ Co, Fe, Mn and $A =$ Nb,Ta) compounds. Recently, extensive research has been devoted towards these compounds due to the discovery of a magnetic-field-induced EP below the magnetic ordering, the mutual manipulation of the magnetic and electric order parameters, as well as a large magnetoelectric coupling constant in $Co_4Nb_2O_9$ [12–15]. Compounds with $M =$ Co, Fe, and Mn crystallize in the trigonal space group $P\bar{3}c1$ (No. 165) with two crystallographically distinct M sites: M1 (0.33, 0.66, z_1) and M2 (0.33, 0.66, z_2). In contrast, $Ni_4Nb_2O_9$, the only Ni counterpart, has two modifications, crystallizing in $Fd2d$ (No. 43) and $Pbcn$ (No. 60), respectively [16]. The crystal structure of these materials is built from alternating layers of M1 and M2 honeycombs. The M1 and M2, which are in the distorted octahedral oxygen cages, form edge-shared coplanar and corner-shared buckled hexagons, respectively, and face-shared octahedra connect these hexagons along c.

This family of compounds was first synthesized and investigated by Bertaut *et al.* [17]. The magnetoelectricity was initially confirmed by Fischer *et al.* measuring the magnetoelectric susceptibility [18]. The long-range ordering

---

[*] narendirakumar.narayanan@anu.edu.au; narennnaren@yahoo.de
[†] yun.liu@anu.edu.au
[‡] Dehong.Yu@ansto.gov.au

temperature increases with the spin quantum number and decreases with the ionic radii of *A* and reaches a maximum value of 109 K for $Mn_4Nb_2O_9$ [14,17]. Possible exchange interactions in $Co_4Nb_2O_9$, $Co_4Ta_2O_9$, and $Mn_4Nb_2O_9$ were discussed by Bertaut *et al.* [17], Osmond *et al.* [19], and, very recently, Solovyev *et al.* [20]. However, several issues regarding the magnetic structure, anisotropy, and magnetic interactions remained debated from the beginning, which are essential for the description of their magnetoelectric properties. The magnetic structures were so far only determined for $M_4Nb_2O_9$ (M = Co and Mn). In particular, the magnetic structure of $Co_4Nb_2O_9$ is surrounded by controversy. According to Bertaut *et al.* [17], the spins order antiferromagnetically along *c* with $k = (0, 0, 0)$ for $Co_4Nb_2O_9$. However, Khanh *et al.* recently showed by single-crystal neutron diffraction on $Co_4Nb_2O_9$ that the spin is ordered in the *ab* plane and canted towards *c* [15]. Very recently, Deng *et al.* [21] determined the ordered spins to be predominantly in the *ab* plane. This casts the question on the origin of the anisotropy, canting, and Dzyaloshinskii-Moriya antisymmetric exchange in this family of materials. For compounds with weak spin-orbit coupling (SOC) as in this family of materials, long-range magnetic dipole-dipole interaction may also play a key role in determining the anisotropy by competing with SOC. Also, regarding the symmetric exchange interaction, doubts remain such as regarding the exchange constant J1 which couples M1 and M2. As these compounds contain partially filled narrow *d* bands, the onsite electron-electron repulsion is significant. However, concerning the influence of electron correlation on the magnetic and multiferroic properties, apart from one low-energy electron model investigation [20], no electronic structure investigation was performed. Such studies would certainly be helpful in understanding and optimizing the multiferroic properties.

In order to elucidate the above issues, we investigate the magnetic structure and the role of spin correlations in determining the magnetic interactions in $Mn_4Ta_2O_9$. For $Mn_4Ta_2O_9$, neither the magnetic structure nor the exchange interactions are known. This is a large $S = 5/2$ spin system where the magnetic coupling effects are enhanced and magnetic frustration effects are limited. This is an ideal system to study the exchange interactions and particularly the effects of the weak long-range magnetic dipole-dipole interaction, due to the very weak SOC expected from a very small orbital polarization. The studies can be easily extended to other members of the whole family of these materials and help to distinguish between the different magnetic models proposed for certain members of the system. Furthermore, Ising or non-Ising critical behavior may also be a fingerprint of the magnetic models, which can be distinguished by determining the critical exponents. The related easy-plane or easy-axis classification, which may be elucidated by investigating the spin-wave excitations (gapped or ungapped mode), can further refine the magnetic model. Here we present our systematic investigation of $Mn_4Ta_2O_9$ by a combination of several different techniques of neutron powder diffraction (NPD), inelastic neutron scattering (INS), heat-capacity measurements, electronic band structure calculations, and spin-wave modeling.

II. EXPERIMENTAL AND CALCULATION DETAILS

Trigonal $Mn_4Ta_2O_9$ was synthesized through solid-state reaction. Chemically pure MnO (99.99%) and Ta_2O_5 (99.99%) were ground together in an agate mortar, pelletized, and kept in a tube furnace in an inert atmosphere at 1200 °C for a total of 60 h with several intermediate grindings to obtain a highly homogeneous powder. No impurities were detected in x-ray powder diffraction. However, negligible amounts of Mn_3O_4 and Mn_5O_8 were found in neutron powder diffraction experiments, which cannot be avoided through the solid-state route [22].

Neutron powder diffraction [NPD, $\lambda = 1.548(1)$Å] experiments on $Mn_4Ta_2O_9$ were performed on the high-resolution neutron diffractometer SPODI of FRM II Garching n. Munich, Germany [23] at selected temperatures from 4 to 300 K to determine the magnetic structures below the magnetic-ordering temperatures and short-range magnetic order. Additionally, laboratory x-ray powder diffraction (XRD) measurements were carried out using Mo $K\alpha1$ radiation with NIST 640d Si ($a = 5.43123$ Å) as an internal standard on a custom-built transmission setup [24]. Low-temperature powder XRD was performed with a sample holder incorporated in a closed-cycle helium cryostat between 25 and 295 K. Rietveld refinements [25] of structural and magnetic parameters were performed, against the x-ray and neutron-diffraction data, using the program FULLPROF [26].

Inelastic neutron-scattering experiments on $Mn_4Ta_2O_9$ were performed with the cold neutron time-of-flight spectrometer PELICAN [27], at the OPAL reactor at Australian Nuclear Science and Technology Organisation (ANSTO), Australia. The incident neutron wavelength is 2.345 Å, corresponding to the second-order reflection from the monochromator through adjusting the phase between two Fermi choppers. The sample was loaded in an annular aluminum can. Measurements were recorded at selected temperatures from 1.5 to 150 K. Data analysis was performed using the program LAMP [28]. The spin-wave modes were calculated with the software SPINW [29], utilizing classical Monte Carlo simulation and linear spin-wave theory for solving the spin Hamiltonian. The exchange parameters for the spin Hamiltonian were obtained from calculations based on density functional theory.

Heat-capacity measurements were performed on a Quantum Design Physical Property Measurement System at selected temperatures from 4 to 200 K.

First-principles density functional theory (DFT) spin-polarized electronic-structure calculations were performed by the full-potential linearized augmented plane-wave plus local orbital method as implemented in the ELK code [30] and in the WIEN2K code [31]. The value of $R_{\mathrm{MT}}K_{\max}$, where $K_{\max}$ corresponds to the largest plane-wave vector and R_{MT} to the smallest atomic sphere radius, was set to 7. The mesh of special *k* points is selected to be 3 × 3 × 3 for total-energy calculations to determine the exchange constants J_i and the magnetic anisotropy energy (MAE), which is proportional to the single-ion anisotropy (SIA), in systems where the easy axis is determined by spin-orbit coupling. For the reproducibility of the MAE, an $R_{\mathrm{MT}}K_{\max}$ of 8 and a *k* mesh of 4 × 4 × 3 were used. The number of independent atoms

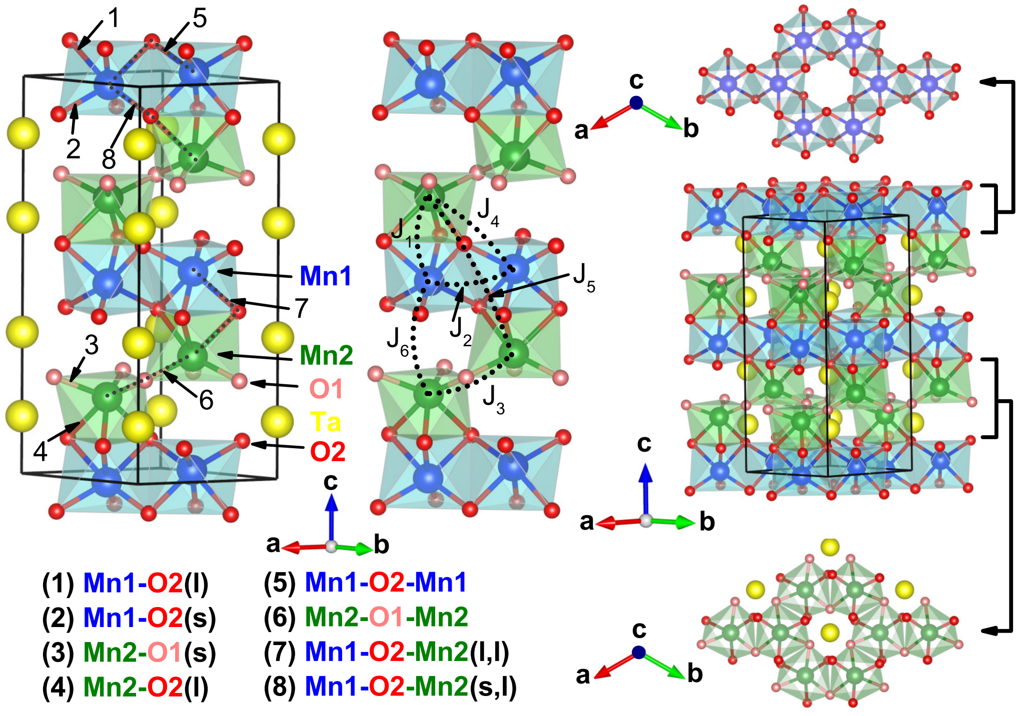

FIG. 1. Unit cell of $Mn_4Ta_2O_9$ containing two formula units (left), relevant exchange paths denoted by exchange constants J_i (middle), and the extended cell exhibiting the flat and buckled honeycomb layers (right). Relevant Mn-O bond lengths and Mn-O-Mn bond angles are also indicated.

in the unit cell is 30 for all calculation. For the exchange-correlation energy functional, the spin-polarized version of the local density approximation (LSDA) was used [32]. For the determination of MAE, PBE [Perdew-Burke-Ernzerhof version of the generalized gradient approximation (GGA)] and PBEsol (a revised version of PBE) were also used [33,34]. The SOC was included in a second variational step with scalar relativistic orbitals from the first variational step as the basis to set up the Hamiltonian for collinear calculations and it was included in the first variational step for noncollinear calculations. The convergence was assumed to be reached when the difference in the total energies became less than 0.0000001 Ry for all calculations. For the optimization of the structural parameters, additionally a convergence criterion based on the forces <2 mRy/a.u. was imposed. The on-site Coulomb repulsion U has been included for the d bands together with exchange parameters J for Mn1 and Mn2 via the fully localized limit (FLL) [35] and around-mean-field (AMF) [36] methods. Again for the calculation of the MAE, several other orbital-dependent potentials apart from LSDA+U, such as orbital polarization [37], on-site exact exchange ($\alpha = 1$) and on-site PBE0 hybrid functional as correction, were applied within the atomic spheres for the d bands [38]. The structural parameters were taken from NPD at 4 K for all calculations (see Table I in the Supplemental Material [39]). The magnetic dipole-dipole interaction energy tensor was calculated for different directions of the magnetic moment of each 8 Mn^{2+} ions within the unit cell to neighbors within 10 Å distance, as described in Ref. [40].

III. RESULTS

A. Nuclear structure

The structural characterization of trigonal $M_4A_2O_9$ was treated by several authors [15,17,18]. $Mn_4Ta_2O_9$ crystallizes in the space group $P\bar{3}c1$ (No. 165) with two crystallographically distinct Mn sites, Mn1 and Mn2, with the oriented site symmetry of 3, which is the same as other trigonal members. For convenience, we describe Mn1 and Mn2 as octahedrally coordinated by oxygen, although both Mn1 and Mn2 are at the common vertex of two oxygen trigonal pyramids, which are oriented along the c axis (trigonal antiprism). Therefore, each octahedron contains two different Mn-O bond lengths, $(\text{Mn-O})_l$ and $(\text{Mn-O})_s$, respectively. The $Mn1O_6$ corner-shared octahedra form a coplanar honeycomb layer, whereas the $Mn2O_6$ octahedra form a buckled honeycomb layer, which are connected along c by face-shared $Mn1O_6$ and $Mn2O_6$ octahedra. This creates different interlayer and intralayer exchange paths and their coupling strengths are influenced by the orientation of MnO_6 octahedra. In agreement with [17,19], we identified four different superexchange paths (Mn-O-Mn, J_1-J_4) and two different super-superexchange paths (Mn-O-O-Mn, J_5 and J_6) (Fig. 1). The space surrounded by the MnO_6 octahedra is occupied by Ta atoms. The unit cell contains two formula units (f.u.) of $Mn_4Ta_2O_9$. The important structural parameters of $Mn_4Ta_2O_9$ at 300 K are listed in Table I.

B. Magnetic structure

Figure 2 shows the temperature dependence of selected Bragg reflections observed by neutron diffraction at low 2θ

TABLE I. Structural parameters of $Mn_4Ta_2O_9$ at 300 K, as determined by neutron powder diffraction. The neutron-diffraction patterns were analyzed by Rietveld [25] refinements using FULLPROF [26]. The resulting R and R_F values are 3.57 and 2.69. The letters "s" and "l" denote the small and large Mn-O bond lengths within an octahedron.

Space group P-3c1					
Lattice parameters					
a (Å)		c (Å)		V (Å^3)	
5.32914 (4)		14.3401 (1)		362.691 (5)	
Ion	Wyckoff	x	y	z	B_{iso}
Mn1	4d	0.3333	0.6666	0.0189 (1)	0.74 (4)
Mn2	4d	0.3333	0.6666	0.3040 (1)	0.90 (4)
Ta	4c	0.0000	0.0000	0.3566 (1)	0.62 (2)
O1	6f	0.2766 (2)	0.0000	0.2500	0.79 (2)
O2	12g	0.3347 (1)	0.3065 (2)	0.0860 (1)	0.91 (1)
Bond lengths (Å)				Bond angles (°)	
Mn1-O2 (l)		2.260 (6)	Mn1-O2-Mn1		89.8 (2)
Mn1-O2 (s)		2.158 (4)	Mn2-O1-Mn2		110.1 (1)
Mn2-O1 (s)		2.098 (3)	Mn1-O2-Mn2 (l,l)		84.2 (2)
Mn2-O2 (l)		2.319 (6)	Mn1-O2-Mn2 (s,l)		126.8 (1)

angles in the temperature range 4 to 300 K (left) and thermal evolution of their integrated intensities (right). Below around $T_N = 105$ K, an increase of the 100 reflection can be seen. Low-temperature x-ray diffraction in this temperature range indicates neither a structural phase transition nor an increase of the 100 reflection. Therefore, the increase in the 100 Bragg reflection observed by neutron diffraction is attributed to magnetic long-range ordering of Mn in $Mn_4Ta_2O_9$.

Two characteristics of the Bragg reflections around the ordering temperature should be mentioned. Diffuse tails on both sides of the 100 reflection already appear around 160 K, which is attributed to lower-dimensional short-range magnetic ordering probably within the honeycombs (see Fig. 1 in the Supplemental Material [39]). However, for an unambiguous determination of the dimensionality, an analysis of the shape of the diffusive peak is required [41]. Second, the 100 reflection itself broadens below T_N, due to the different correlation length of magnetic long-range ordering (see Fig. 1 in the Supplemental Material [39]). The magnetic structure can be described by the propagation vector $k = (0, 0, 0)$. The magnetic unit cell is identical to the crystallographic unit cell. This k vector is the prevalent one in this family of materials and has been determined for several other members [15,17]. The direction of the magnetic moment, however, differs from compound to compound and can be easy axis, easy plane, or even more complicated [15,17]. The increase of the 100 reflection compared to 002 indicates that the moments orient along c thus forming an easy-axis system [Fig. 2 (right)] for $Mn_4Ta_2O_9$. Furthermore, for the quantitative determination of the magnetic structure, we performed Rietveld [25] refinement based on representational analysis [42,43]. The lower angle regions of the observed and calculated diffraction

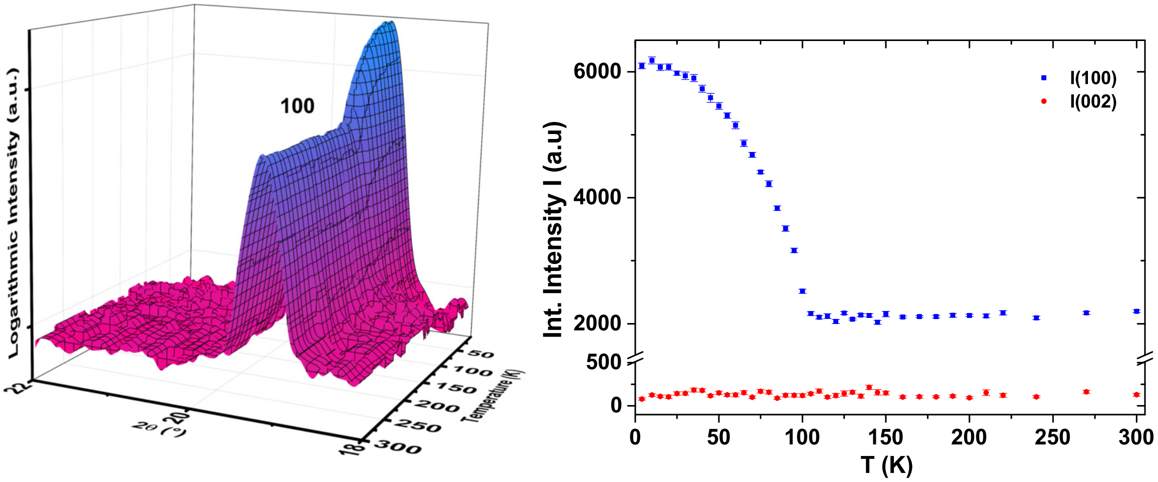

FIG. 2. Temperature dependence of the lower-angle Bragg reflection 100 in the temperature range 4 to 300 K (left) and the integrated intensities of 100 and 002 (right) (neutron data).

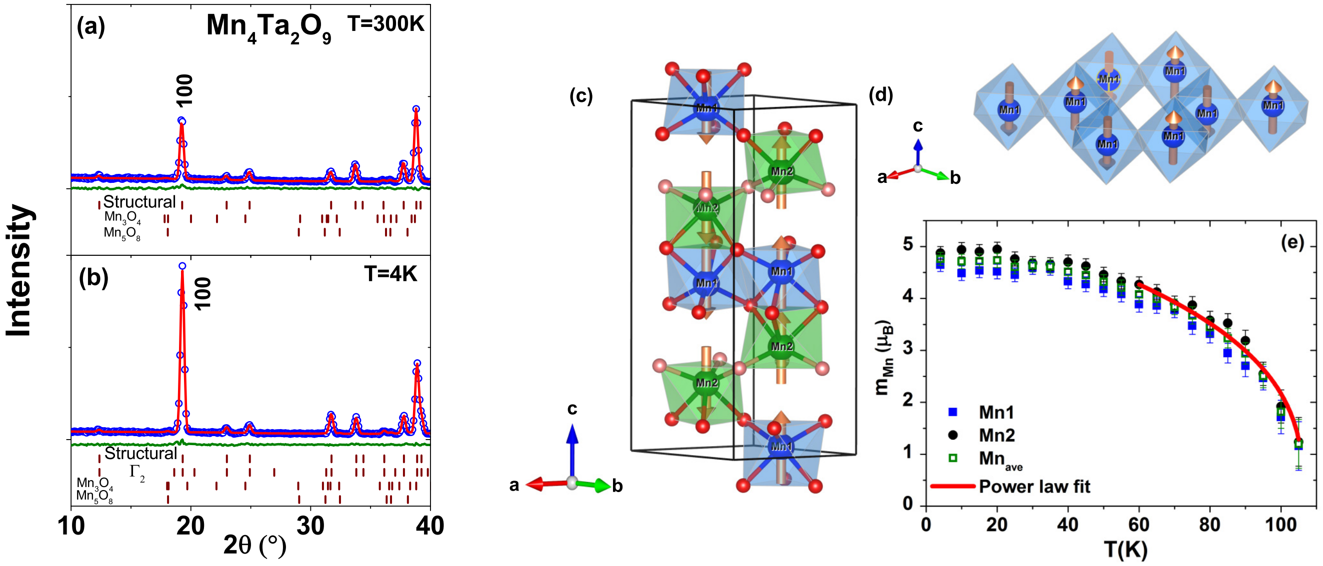

FIG. 3. (a),(b) Observed (blue open circles) and calculated (red solid lines) neutron powder diffraction patterns for $Mn_4Ta_2O_9$ in the 2θ region where prominent Bragg reflections are present, which are purely a structural contribution in the paramagnetic phase at 300 K and structural plus magnetic contribution at 4 K. Reflection markers correspond to the positions of Bragg reflections of structural, magnetic ($\Gamma_2 = \Gamma_4^P$), and minor impurity contributions (Mn_3O_4 and Mn_5O_8). (c) Magnetic structure of $Mn_4Ta_2O_9$ in the unit cell and (d) within the Mn1 honeycomb. (e) Magnetic moment of Mn1, Mn2 and the average moment M_{ave}. The baseline for the power-law fit was selected to be the x (temperature) axis.

patterns, which contains the prominent Bragg reflections for $Mn_4Ta_2O_9$ at 300 and 4 K, are shown in Figs. 3(a) and 3(b) (left).

For $k = (0, 0, 0)$, all 12 symmetry elements of $P\bar{3}c1$ belong to the little group G_k, resulting in four real one-dimensional and two complex two-dimensional irreducible representations. For the trial of the possible magnetic structures, we transformed the two complex two-dimensional irreducible representations to real physically irreducible representations via a unitary transformation. Details related to the analysis of the magnetic modes are summarized in the Form. C1, Tables II and III in the Supplemental Material [39]. The magnetic ordering of the Mn moments below T_N is successfully described by the basis vectors of the one-dimensional irreducible representation Γ_2 (Γ_4^P) for the $4d$ site for both Mn1 and Mn2. As qualitatively described above, the Mn moments are ordered along c. The neighboring Mn moments are ordered antiferromagnetically within the respective honeycombs, while between the honeycombs the adjacent Mn moments are ordered ferromagnetically [Figs. 3(c) and 3(d)]. It should also be noted from the magnetic modes in Table III in the Supplemental Material [39] that the canted magnetic structure as described by Khanh *et al.* for $Co_4Nb_2O_9$ is not realized using the basis functions of single irreducible representations, as for the first four irreducible representations the moments are along c and for the two two-dimensional ones the moments are confined to the ab plane. However, considering exchange multiplets and combining the one-dimensional and two-dimensional irreducible representations, such an ordering is realizable ($\Gamma_4^P + \Gamma_6^P$) [44]. The refined magnetic moments of Mn^{2+} for Mn1 and Mn2 are 4.7(1) μ_B and 4.8(1) μ_B, respectively, and they are close to the high-spin $S = 5/2$ state for Mn^{2+}. A power-law fit of the temperature dependence of the average Mn moment Mn_{ave} was performed and the T_N and the critical exponent β were determined to be 106.4(9) K and 0.34(3) K, respectively. However, the critical behavior of the magnetic system cannot be unambiguously determined from β alone as the obtained value is close to three-dimensional Ising, XY, and Heisenberg models [45]. Therefore, the further critical exponent α from heat-capacity measurements has to be explored to distinguish between the models. This will be described in the heat-capacity section.

C. Exchange striction

The temperature dependences of the lattice parameters and volume of the unit cell of $Mn_4Ta_2O_9$ are shown in Fig. 4. The temperature dependency of the structural parameters contains information on the coupling of the spin to lattice through magnetostriction [Figs. 4(a)–4(c)]. In the paramagnetic phase, the lattice parameters a and c follow the usual thermal expansion characteristics and decrease with decreasing temperature. The data above 160 K was fitted with the Debye-Grüneisen and Einstein thermal-expansion models [46–48] for a, and c and the volume of the unit cell are extrapolated to the magnetically ordered region. Deviation from the usual thermal expansion due to the phonon contribution sets in around 130 K for a and the volume, and around T_N for c. This demonstrates that the magnetic short-range ordering above T_N is limited to the ab plane, within the honeycombs. Whereas a and the volume undergo a rapid decrease, c increases relative to the models. These deviations can be explained by the magnetic structure of $Mn_4Ta_2O_9$ in Fig. 3. The rapid reduction of a is due to the symmetric exchange striction caused by the antiferromagnetic coupling within the ab plane, within the honeycomb layers [see Fig. 2 in the Supplemental Material

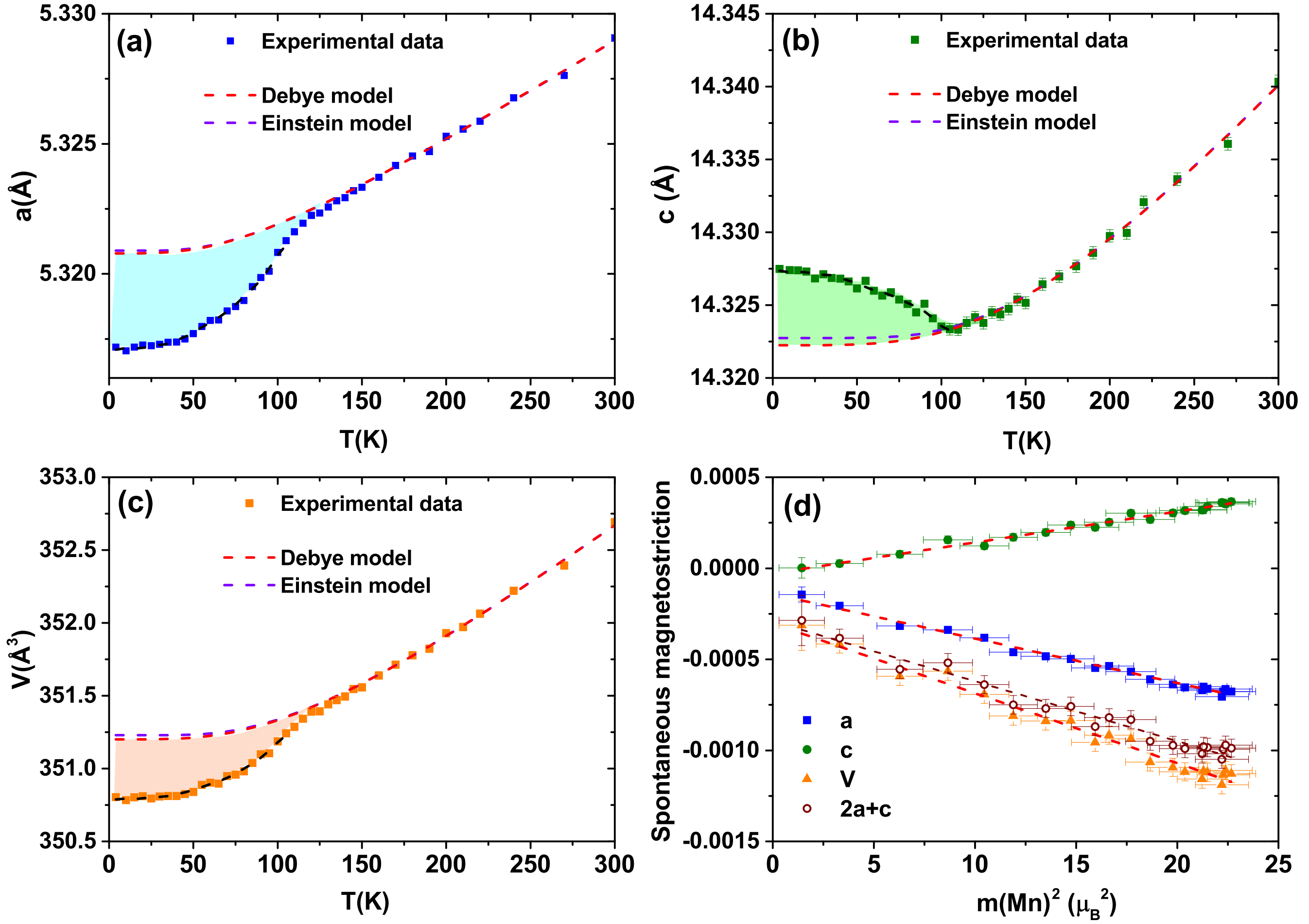

FIG. 4. (a)–(c) Temperature dependence of the lattice parameters a and c and the volume of the unit cell of $Mn_4Ta_2O_9$. The fits of the experimental data to the Debye-Grüneisen and Einstein models in the paramagnetic phase are shown by red and violet dashed lines, respectively. The black dashed lines in the AFM phase are the deviation of the parameters recalculated from the exchange-striction coefficients and the square of the magnetic moment. (d) Magnetic moment dependence of the spontaneous magnetostriction of various structural parameters and their linear fits (dashed lines).

[39] for Mn2-O1 (s)]. The expansion of c is the result of the symmetric exchange striction caused by the ferromagnetic coupling particularly along the Mn1-O2-Mn2 (l,l) bond (see Fig. 2 in the Supplemental Material [39]) in the c direction. As the magnetic reflections coincide with the nuclear reflections in the NPD pattern, we verified the anomalies in the lattice parameters due to magnetostriction by performing low-temperature laboratory x-ray powder diffraction (XRD) measurements and the results are shown in Fig. 3 in the Supplemental Material [39]. The linear relationship between the spontaneous magnetostriction, calculated from the experimental data with the Debye-Grüneisen model as in Ref. [46], and the square of the average Mn magnetic moments within the symmetric exchange, in Fig. 4(d), certify that the magnetostriction can be identified as exchange striction in this compound. Furthermore, the small difference between the volume magnetostriction and the sum of $2a + c$ magnetostrictions indicates the presence of a small anisotropy, which will be addressed in the following sections. Again the magnetostriction for a has a significant nonzero value for $m(\mathrm{Mn})^2 = 0$, indicating that the magnetic short-range ordering above T_N lies within the ab plane. The black dashed curves in Figs. 4(a)–4(c) were recalculated from the symmetric exchange model (square of the average magnetic moments) with the magnetostriction coefficients.

D. Electronic structure

Electronic-structure calculations have been carried out based on DFT. We start with the density of states (DOS), which gives information on the orbital occupations and positions, followed by calculation of magnetic interactions, determining the relative orientation of the moments. The origin of different directions of the magnetic moment has also been explored. Special emphasis is given to the role of electron correlation in this system.

The total density of states (total DOS) and the partial DOS of the Mn d bands calculated with LSDA and LSDA $+ U +$ (J) methods are shown in Fig. 5, respectively. The partial DOS of the $3d$ orbitals of Mn are obtained by projecting the DOS on the d states with the basis of real orbitals. The coordinate system for the projection is selected to be along the diagonals of the Mn1 and Mn2 octahedra and approximated to be orthogonal. The partial DOS exhibits a large bonding anti-

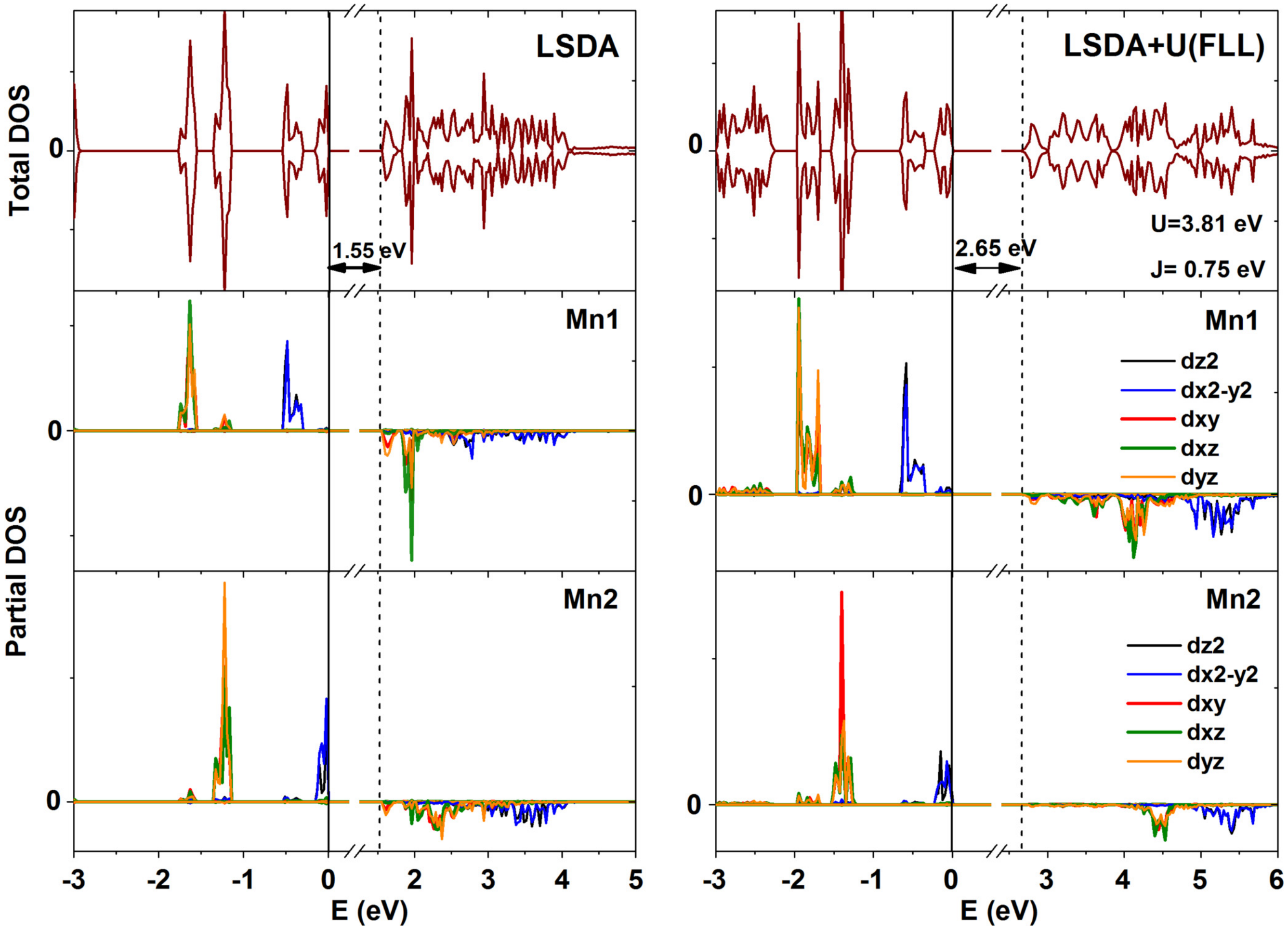

FIG. 5. Total and d-band partial density of states (DOS) of $Mn_4Ta_2O_9$ for the LSDA (left) and LSDA+U(FLL)+J (right). We summarize the (d_{z^2}, $d_{x^2-y^2}$) and (d_{xy}, d_{xz}, d_{yz}) bands as e_g and t_{2g} manifolds, respectively.

bonding splitting (bonding d manifold below -3 eV, which is not shown) and especially the (localized) antibonding bands are further split into the e_g (d_{z^2}, $d_{x^2-y^2}$) and t_{2g}(d_{xy}, d_{xz}, d_{yz}) manifolds in the crystal field. Splitting within the e_g and t_{2g} manifolds due to the lower symmetry than cubic are, however, negligible. This is in good agreement with the schematic crystal-field splitting shown in Ref. [20] for $Co_4Ta_2O_9$ by a model calculation. A strong Hund's coupling results in a high-spin state for Mn^{2+} and the spin polarization between the majority and minority bands results in a band gap of 1.55 eV for the LSDA case. From the partial DOS, the approximate widths of the d bands could be determined, which are important to predict the role of on-site electron-electron interaction in highly correlated systems. They are 0.25 and 0.22 eV for e_g and t_{2g}, respectively, for Mn1, while for Mn2 they are 0.16 and 0.22 eV, respectively. The striking difference is the additional localization of the e_g manifold for Mn2 due to the buckled nature of the Mn2 honeycomb and the reduced nature of the charge transfer. This also has a consequence for the relative energies of the d bands and resulted in a difference in the energy of the d bands between Mn1 and Mn2 due to the different Coulomb repulsions even within the LSDA, which is also seen in Ref. [20] for $Co_4Ta_2O_9$. Both the e_g and t_{2g} manifolds of Mn1 and Mn2 have contributions to the partial DOS at each other's energy range, reflecting the exchange between Mn1 and Mn2. The above obtained bandwidths for e_g and t_{2g} manifolds are smaller compared to the typical values for the on-site (screened) electron-electron Coulomb repulsion of the order of a few eV [49]. Therefore we added an orbital-dependent correction to the on-site Coulomb repulsion with the LSDA + U + (J) method. For the LSDA+U approach, we only consider the fully localized limit (FLL) flavor for the present discussion, as the magnetic penalty term [50] reduced the magnetic moment of Mn^{2+} to a smaller value for the around-mean-field (AMF) flavor. The typical values for U ($3.81\,\mathrm{eV} = 0.28\,\mathrm{Ry}$) and J ($0.75\,\mathrm{eV} = 0.055\,\mathrm{Ry}$) were taken from [49]. Adding the LSDA+U correction increases, as expected, the band gap to 2.65 eV (for $U = 3.81\,\mathrm{eV}$ and $J = 0.75\,\mathrm{eV}$) and emphasizes the role of electron correlation in this class of materials (the DOS for LSDA + $U = 6.12\,\mathrm{eV}$ (0.45 Ry) is shown in Fig. 4 in the Supplemental Material [39]). The inclusion of U shifts the occupied spin-up d bands (both e_g and t_{2g}) by $-(U - J)/2$ and the unoccupied spin-down d bands by $+(U - J)/2$, as evident from Fig. 5. Here, J accounts for the already considered repulsion between the parallel spins due to the Pauli principle (exchange

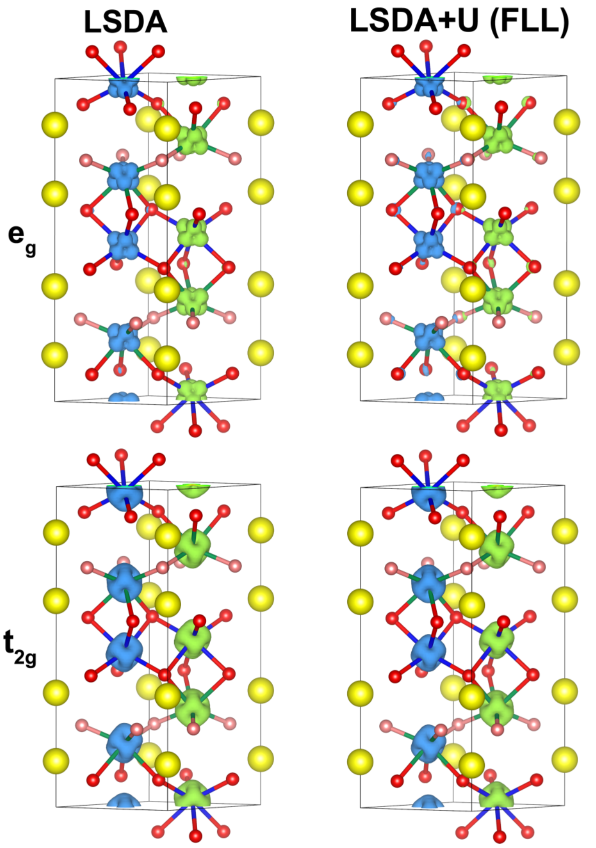

FIG. 6. Spin-density isosurfaces at 0.25 and −0.25 $\mu_B/\text{Å}^3$ of the e_g and t_{2g} manifolds of Mn1 and Mn2, calculated for the LSDA and LSDA+U cases for the AFM structure obtained from NPD. The positive and negative spin densities are characterized by blue and green colors, respectively.

hole). Therefore, this compound can be classified as a Mott insulator.

The spin densities are shown in Fig. 6. The different signs of the spin density are illustrated by different colors (blue and green). The e_g and t_{2g} manifolds are clearly visible in Fig. 6 demonstrating the localized character of the bands. For the LSDA+U case, additionally a spin polarization of the oxygen is also visible. The calculated spin and orbital moments are shown in Table II. It is evident that the Mn on each site tend to be in a high-spin $S = 5/2$ state with more localization achieved after adding corrections to the electron correlation through LSDA+U. However, the spin moments on each site are less than the expected value of 5 μ_B/Mn^{2+} in the high-spin state even after the addition of U. This is assumed to be mainly due to the hybridization with O as seen from the contribution of the d bands to the bonding part of the partial DOS. They are in good agreement with the NPD results of 4.7 μ_B/Mn^{2+}, even for the LSDA+U case. A slight discrepancy exists between the collinear calculations and noncollinear calculations, where the spin moments are allowed to rotate freely (although the Mn moments remained rigidly coaligned), due to the missing contributions to the noncollinear system such as Dzyloshinski-Moriya or anisotropic exchange (pseudodipolar). The orbital moments were calculated with SOC included. The obtained values for the orbital moments are very small, emphasizing the weak effect of SOC in this system (the inclusion of SOC neither changes the band gap nor induces a relativistic splitting of the bands and the only effect is a slight change in the spectral weight of the DOS due to the coupling between majority and minority spins; see Fig. 4 in the Supplemental Material [39]). In addition, the sign of the weak orbital moment changes depending on whether the spins are collinear or noncollinear. Towards the end of this section, we will investigate the role of this "weak" SOC in determining the direction of the magnetic moment and the influence of electron correlation on the SOC.

The total energies for different spin configurations for LSDA and LSDA+U are shown in Table III. It is evident that the experimentally obtained magnetic structure (AFM, GS) belongs to the most stable structure with the least energy (other configurations are shown in Fig. 5 in the Supplemental Material [39]). However, we cannot distinguish between Γ_4^P, Γ_6^P, and the exchange multiplet $\Gamma_4^P + \Gamma_6^P$ (without canting). Therefore, it can be said that within the isotropic Heisenberg model, both LSDA and LSDA+U predict the experimentally obtained magnetic structure. We added SOC in different directions, which couples the spin space with the crystal lattice and determines the SIA and the associated MAE in single-ion-determined anisotropy systems. We will come to those results towards the end of this section.

The effect of the electron correlation is also reflected in the calculated exchange parameters, which are shown in Table IV. These are calculated by two different methods, the configuration method (CM) and the two-spin method (TSM) [51,52], which are explained in Form. C2–C4 in

TABLE II. Calculated spin (m_s) and orbital (m_L) moments for LSDA with different corrections.

		LSDA	LSDA+U(FLL)	LSDA+SOC(c)	LSDA+SOC(a)	LSDA+SOC(c)+U	LSDA+SOC(a)+U
				Noncollinear			
Mn1	m_S	4.37	4.55	4.37	4.37	4.55	4.55
(μ_B)	m_L			0.0008	0.0013	0.0002	0.0007
Mn2	m_S	4.34	4.53	4.33	4.33	4.53	4.53
(μ_B)	m_L			0.0005	0.0020	0.00004	0.0010
				Collinear			
Mn1	m_S	4.23				4.40	4.40
(μ_B)	m_L					–0.00118	–0.00236
Mn2	m_S	4.20				4.38	4.38
(μ_B)	m_L					–0.00167	–0.00269

TABLE III. Total-energy differences ΔE given relative to the experimentally observed $k = (0, 0, 0)$ antiferromagnetic structure, denoted as AFM, GS, in meV/unit cell, for ferromagnetic (FM) and for five other different antiferromagnetic (AFM) configurations with $k = (0, 0, 0)$. One unit cell contains two formula units (f.u.) of Mn$_4$Ta$_2$O$_9$. The J value was selected to be $J = 0.75$ eV.

ΔE (meV/unit cell)	AFM,GS	FM	AFM2	AFM3	AFM4	AFM5	AFM6
LSDA	0	+996.5	+549.8	+188.0	+493.5	+359.9	+372.5
LSDA + U(FLL) = 3.81 eV + J	0	+428.2	+223.7	+69.0	+229.9	+157.0	+169.8

the Supplemental Material [39]. It is evident from Table IV that the strongest exchange interactions lie within the honeycombs reflected by the larger values of J2 and J3. The interhoneycomb exchange parameters J1 and J4, which connect the different honeycombs, represent the next strongest interactions. J5 and J6, which are of the type M-O-O-M, are much weaker than M-O-M (J1–J4) exchange. Note that the calculated J1 is antiferromagnetic, whereas the magnetic moments are ferromagnetically ordered along the exchange path of J1. This may be due to the polarization of the O 2p states not being considered [53]. The stronger J2 and J3 within the honeycombs explain the magnetic diffuse features above the long-range ordering temperature. Adding a U parameter almost halves the values of the exchange parameters obtained for LSDA but retains the ratio between them. With increasing U, the splitting between the occupied and unoccupied bands become larger due to the increased on-site electron-electron interaction and therefore reducing the exchange constants. The ordering temperature (∼561 K) obtained by a "molecular" mean-field approximation (MFT) is clearly much higher than the experimental one for the LSDA case, whereas the ones obtained for the LSDA+U case significantly reduce the T_N due to the shifting of the occupied band downwards and the unoccupied bands upwards. The T_N values are still higher than the experimental value of 102 K even for the LSDA+U case. This is primarily due to the fact that the MFT does not include fluctuations and therefore overestimates the ordering temperature [54,55]. As discussed above in another context, not considering polarization of the O 2p states may also have overstrengthened the antiferromagnetic exchange. Lastly, although LSDA+U increased the band gap and reduced the exchange constants, electron correlation is treated in the static limit which lacks dynamic screening through fluctuation. Comparing with other members such as Co$_4$Nb$_2$O$_9$, apart from J1 the relative strength of the exchange parameters is in good agreement [20]. The large discrepancy between the J1 values come from the fact that Co^{2+} has only one t_{2g} exchange orbital compared to three in the case of Mn^{2+}.

In the final part of this section, we elucidate the origin of the interactions which determine the direction of the magnetic moment. For this purpose, first we investigate the effects of SOC, which couples the spin space to the lattice and enables a direction for the magnetic moment in SIA systems. From Table II, it is evident, due to the small magnitude of the orbital moment, that SOC is a weak effect in this system. It also allows us to compare the experimentally determined magnetic structure Γ_4^P with the direction of the quantization axis with the least energy in calculations, as apart from Γ_4^P, Γ_6^P and $\Gamma_4^P + \Gamma_6^P$ also have the same structure within the isotropic Heisenberg model. Another interesting question is about any influence on SOC from the on-site electron-electron repulsion. The results are shown in Fig. 7.

For the LSDA case, rotating the SOC direction from [001] towards [100] and [110] (characterized by θ), the energy difference ΔE has the same trend. In both cases, [100] and [110] have the least energy. The energy difference ΔE due to the rotation of the SOC within the ab plane is negligible and therefore magnetic moments rotated anywhere onto the ab plane have the least energy. This is in contrast to the direction of the magnetic moment determined by NPD ($\Gamma_2 = \Gamma_4^P$) to be along c. The MAE for LSDA is quite high and is around 0.8 meV/f.u. As this is a highly correlated electron system as discussed above, we switched on the on-site electron-electron Coulomb repulsion U within the FFL flavor. For the U and J values, initially 3.81 and 0.75 eV were applied, which were taken as above from [49]. For these values, the MAE was reduced to almost half of its value for LSDA. Further increase of U resulted in further reduction in MAE and reached a value of around 0.2 meV/f.u. for $U = 10$ eV (not shown), which is the high limit for realistic calculations. Although U was unable to force [001] towards the least-energy direction, it strongly reduced the barrier between [100] and [001] towards a disfavoring of the moments along [100]. Therefore, the strong influence of the electron correlation on the SOC is evident for Mn$_4$Ta$_2$O$_9$, which is known for other systems [56]. Replacing LSDA with different forms of GGA such as PBE and PBEsol did not improve this energy difference, as with the other

TABLE IV. Exchange constants J_i in meV and the magnetic ordering temperature T_N calculated utilizing the molecular field theory (MFT). The configuration method and the two-spin method are denoted by CM and TSM, respectively.

Exchange constants (meV)	J$_1$	J$_2$	J$_3$	J$_4$	J$_5$	J$_6$	T_N (K) MFT
LSDA (TSM)	2.309	3.702	4.839	2.014	0.106		561.00
(CM)	3.131	3.713	4.811	2.303	0.155	0.019	561.84
LSDA + U(FLL) = 3.81 meV + J(TSM)	0.945	1.833	2.120	0.794	0.054		249.90
(CM)	1.316	1.804	2.078	0.891	0.045	−0.023	244.22
LSDA + U(FLL) = 5.44 meV(TSM)	0.667	1.371	1.588	0.530	0.123		183.35
LSDA + U(FLL) = 6.12 meV(TSM)	0.608	1.239	1.556	0.459	0.115		169.63

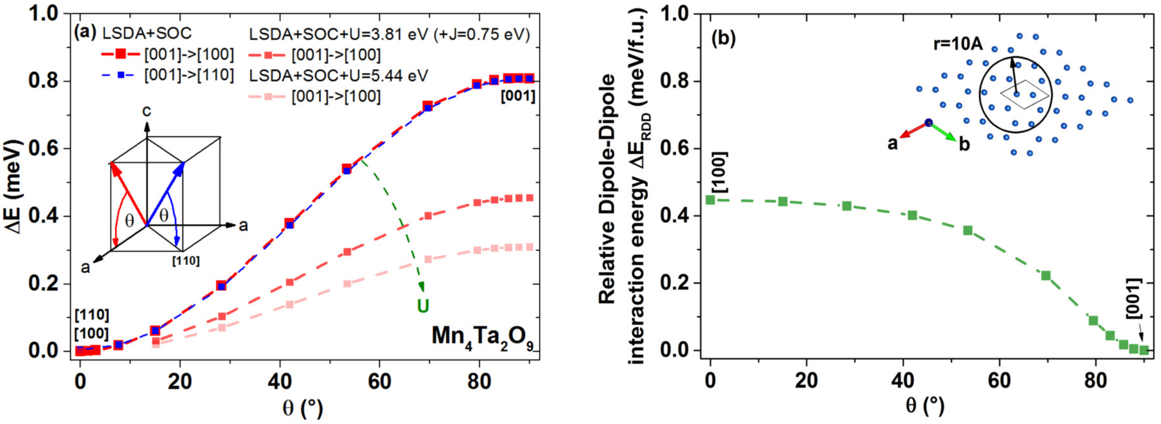

FIG. 7. (a) Energy difference for LSDA+SOC+U, for SOC rotated towards different directions and for different U. In this case, $\Delta E = E(001)$-$E(100)$ is the MAE. (b) Relative dipole-dipole interaction energy ΔE_{RDD} for the rotation of the moments within the *ac* plane. With increasing U, [001] becomes energetically favorable ($\Delta E_{\mathrm{RDD}} + \Delta E$) over [100].

orbital-dependent potentials apart from LSDA+U(FLL), such as orbital polarization (Hund's second rule correction), on-site exact exchange ($\alpha = 0.25$), and on-site hybrid functional ($\alpha = 0.25$), as correction for the deficiencies of LSDA. Application of these "other" orbital-dependent potentials and the AMF flavor of LSDA+U even significantly increased the ΔE between [100] and [001], thus favoring [100]. We investigated further the dependency of the MAE on the volume modification. The MAE decreases with increasing volume; however, even in the upper limit of a realistic U (10 eV), SOC along [100] is slightly energetically more favorable than [001] (see Fig. 6 in the Supplemental Material [39]). It should also be noted that although the calculated magnetic moment of Mn is close to the experimental value, it is still smaller than 4.7 μ_{B}/Mn refined from NPD even at the FLL. This reduction is also known from other oxides containing Mn^{2+}, appearing at first sight to be due to hybridization effects [57]. In this context, it should also be noted that the correlation and screening as in the LSDA+U were considered in the static limit. Therefore, dynamical correlation and screening effects, which are considered in methods such as dynamical mean-field theory or its combination with GW [58–60], might be required to further influence the barrier, favoring [001]. But for the moment we assume that SOC is solely unable to reproduce the experimental direction of the moment.

In several compounds, where the magnetism originates from 3d orbitals and with a weak SOC, long-range magnetic dipole-dipole interaction can either compete with the SOC or work together with the SOC in determining the direction of the magnetic moments [61–63] (see Form. C5 in the Supplemental Material [39]). For a large-spin system as $S = 5/2$, a significant contribution from the magnetic dipole-dipole interaction can be expected. We calculated this contribution for the spins of the eight Mn^{2+} ions in the unit cell with its neighbor Mn^{2+} spins within the radius of 10 Å. After determining the dipole-dipole interaction tensor, we calculated the eigenenergies by varying the direction of the moments within the *ac* plane as for SOC. The results are shown in Fig. 7(b) and the energies are plotted relative to the value along [001] (ΔE_{RDD}). In contrast to the SOC associated total-energy differences ΔE [Fig. 7(a)], the dipole-dipole interaction gives the most favorable moment direction along [001]. In this case, the dipole-dipole interaction competes with SOC in determining the moment direction. However, when comparing with the LSDA+SOC ΔE, the dipole-dipole interaction contribution ΔE_{RDD} is unable to compensate the energy difference and thus [100] remains the favorable direction (Fig. 7). When switching on the on-site electron-electron repulsion U, the MAE is reduced within LSDA+SOC+U and $\Delta E_{\mathrm{RDD}} + \Delta E$ becomes comparable for both [100] and [001] with $U =$ 3.81 eV. For further increase of U (5.44 eV), [001] becomes more favorable over [100]. Therefore, the long-range dipole-dipole interaction together with a strong electron correlation is the driving force in determining the direction of the magnetic moment and the magnetic anisotropy in Mn$_4$Ta$_2$O$_9$.

E. Heat capacity

The temperature dependence of the heat-capacity data and the magnetic contribution to the heat capacity divided by T are shown in Fig. 8. The magnetic contribution was extracted by subtracting the phonon contribution to the specific heat. For this purpose, the Debye model for acoustic phonons, which was approximated by Simpson's rule (see Form. C6 in the Supplemental Material [39]), was fitted to the high-temperature data and extrapolated to the lower-temperature range. The Debye temperature Θ_{D}, which separates the collective motion of ions from the individual motions, was determined from the fitting to be around 452 K, which is typical for a compound with lighter atoms such as O and strong interionic bonding.

A λ-shaped peak is seen around the magnetic ordering temperature $T_N \sim 100$ K [inset Fig. 8(a)], indicating that this transition is of second order. T_N was accurately determined by fitting the formula for the critical exponent α (power law) for second-order phase transitions to the data. The determined T_N and the critical exponent α are 102.1(1) K and +0.17(1) K, respectively. α is closest to a three-dimensional Ising model in the critical region and therefore uniaxial, which forbids canting and is in agreement with our magnetic model. It is also evident, from Fig. 8, that the magnetic contribution extends beyond T_N up to around 150 K. This is attributed

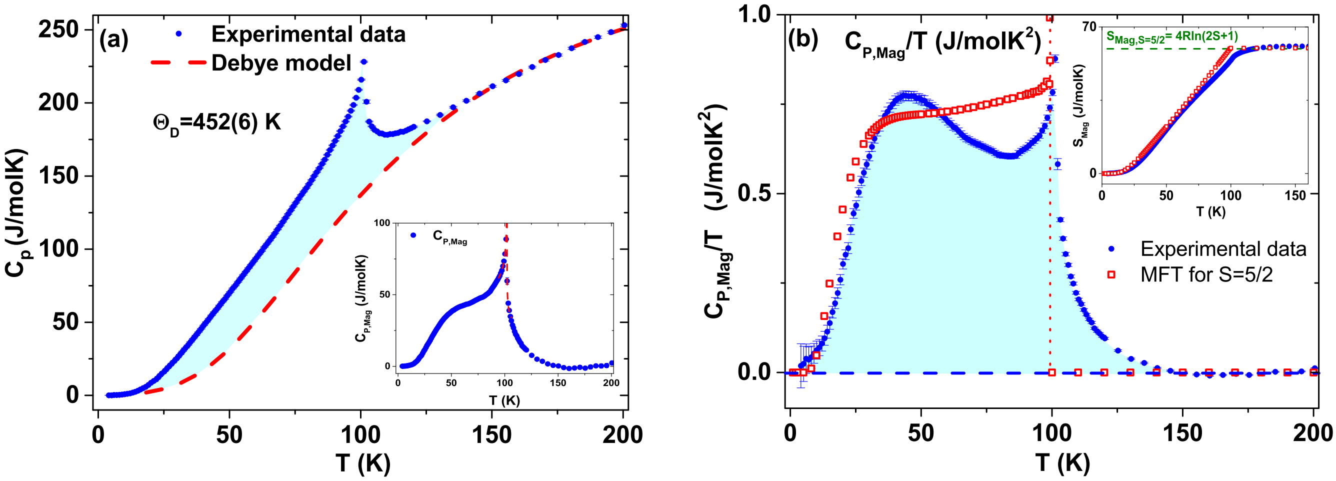

FIG. 8. (a) Temperature dependence of the heat capacity (C_P) with the inset showing the magnetic contribution with a power-law fit (dashed curve within the inset) to determine the critical exponent α. The dashed curve is the phonon contribution approximated by the Debye model. (b) Magnetic contribution of the heat capacity divided by T, $C_{P,\mathrm{Mag}}/T$ together with the MFT approximation and with the inset showing the magnetic entropy S_{Mag}.

to the short-range magnetic ordering which exists within the individual honeycombs above T_N. Caution should be taken in interpreting this as in similar Mn^{2+} systems, such as $\mathrm{BiMn_2PO_6}$, because a phonon softening occurs a long way above T_N and a subtraction of the phonon contribution modeled by a simple Debye model did not consider such effects and overestimated the magnetic contribution [64]. This problem was overcome by measuring a nonmagnetic material with similar structure and ions, such as $\mathrm{BiZn_2PO_6}$, for phonon subtraction. In our case, $\mathrm{Zn_4Ta_2O_9}$ is such a candidate. The magnetic entropy $S_M = \int C_{P,\mathrm{Mag}}/T\, d\mathrm{T}$, which is the contribution from the changes in the magnetic state, is shown in the inset of Fig. 8(b). The magnetic long-range ordering transition is clearly visible in S_{Mag}. With $S_{\mathrm{Mn}} = J_{\mathrm{Mn}} = 5/2$ being the total magnetic moment of Mn^{2+}, a total magnetic entropy of 59.59 J/mol K can be expected theoretically for a f.u. with 4 Mn^{2+} ions. The experimental S_{Mag} reaches a value of 55.8 J/mol K at T_N and saturates at around 145 K with a value of 60.8 J/mol K. This is in very good agreement with the theoretical value. This indicates, on the one hand, that our Debye model for the phonon contribution worked very well due to a nonsignificant softening of Θ_{D} and, on the other hand, that the contribution to the S_{Mag} above T_N comes from the melting of the short-range order within the honeycombs.

Now let us concentrate on the hump around 40 K. This is expected to be due to the splitting of the degenerate Zeeman levels in the molecular field of other Mn^{2+} moments and the temperature-dependent population of the next higher Zeeman level. In order to test this, we calculated the magnetic contribution $C_{P,\mathrm{Mag}}$ using the molecular field theory (MFT) for a $S = 5/2$ system. Indeed, we were able to reproduce the hump around 40 K. We adjusted the theoretical T_N to be around 100 K. This effect is more pronounced for larger S [65]. The MFT solution for S_{Mag} saturates at T_N as fluctuations are not included and the short-range magnetic entropy is compensated by a higher value of C_P below T_N. Apart from that, MFT also does not include spin waves, leading to discrepancies at very low temperatures. We fitted the C_{Mag} at the lower temperature range below 30 K with the formula (8) given in Ref. [66] to predict/extract the value of a possible spin gap (due to the easy-axis system) in the magnetic excitation spectrum. The determined gap is around 3.7(6) meV and we will compare this value with the inelastic neutron data and spin-wave simulation.

F. Inelastic neutron scattering

Inelastic neutron-scattering experiments were performed in order to investigate the spin dynamics in this system and to verify further our magnetic model which was constructed in the previous sections. An INS intensity spectrum collected at $T = 1.5$ K is shown in Fig. 9(a). Compared to the spectrum obtained at 150 K [Fig. 10(a)], spin waves propagating from magnetic Bragg peaks, especially from 001, are clearly visible at 1.5 K. A spin gap cannot be recognizable from the spectrum due to the weak intensity, and the propagation of acoustic phonons at lower-energy transfers is probably from spin lattice coupling. These spin waves reach up to a maximum energy transfer of around 10 meV. Another spin-wave spectrum starts to appear above 13 meV, which is around the maximum energy transfer reachable in the current experiment. This appears to be a gapped mode. Additionally, a weak feature can also be observed around the energy transfer of 6 meV. The energy-transfer dependence of the q summed intensity [Fig. 10(a)] gives an overview of the temperature dependence of the spin-wave modes. Three spin-wave modes are clearly visible with energy around 6, 10, and 13 meV (to highlight the existence of a spin-wave mode around 13 meV, a comparison of the q summed intensity at 1.5 K and with 150 K is shown in Fig. 7 in the Supplemental Material [39]). Up to around 4 meV, there is hardly any intensity contribution below 10 K, indicating an energy gap as predicted before from heat-capacity data. With increasing temperature, the intensity of the spin-wave modes become smaller and the peaks become broader, before they vanish above 100 K in the background of the phonon modes. The powder-averaged spectrum limits

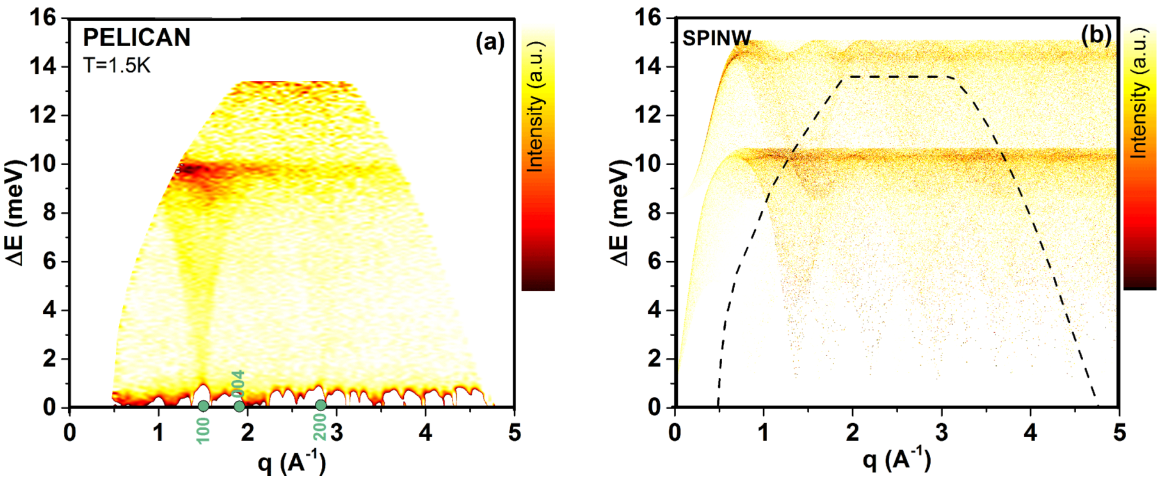

FIG. 9. (a) TOF inelastic neutron-scattering intensity spectrum, in dependence of energy transfer (ΔE) and momentum transfer (q), in arbitrary units measured at $T = 1.5$ K. (b) Powder-averaged simulated intensity spectrum calculated by SPINW, in arbitrary units from the exchange parameters J_i obtained for the LSDA + $U = 6.12$ eV (0.45 Ry) case and from an easy-axis anisotropy $D_{zz} = 0.01$ meV. The broken lines in (b) denote the experimentally available ΔE-q space for our experiment setting.

further interpretation of our data. Therefore, we turned to simulations based on linear spin-wave theory and the classical Monte Carlo method as in SPINW.

The simulated spin-wave spectra along different directions are shown in Fig. 11(a). The exchange parameters for the spin Hamiltonian were taken from DFT calculations from previous sections. As the definition of SIA is a matter of controversy in our system, due to the anisotropy mainly determined by electron-correlation-assisted magnetic dipole-dipole interaction instead of SOC, we started our simulation nevertheless with a very small value of $D_{zz} = 0.01$ meV as an easy-axis anisotropy and the J values from the LSDA + U = 6.12 eV (0.45 Ry) case. There are altogether eight spin-wave modes with each twice degenerate, corresponding to the 8 Mn ions in the unit cell. From the four nondegenerate modes, only two contribute to the intensity corresponding to $S_\perp(q,\omega)$. The spin-wave modes are characterized by blue colored curves and the intensities are scaled by a color map. Most of the intensities are concentrated around the maxima of the modes (or local minima), in very good agreement with the experimental spectrum, corresponding to the features around 6, 10, and above 13 meV. The maxima of the higher-lying spin-wave mode are around 14 meV and mostly missed in our experimental spectrum, but its beginning can be clearly seen. We also created a powder-averaged simulated spectrum, which is seen in Fig. 9(b). All three spin-wave features are in very good agreement with the experimental spectrum. The most important feature of the simulated spin-wave modes is the appearance of a spin gap of around 1 meV even for a perturbation through a very small anisotropy of 0.01 meV. This is consistent at all propagations. Therefore, both intensity modes are gapped modes in this system. It is interesting to see from which component of the spin-wave excitation the intensities originate. This is shown in Fig. 11(b) and the intensities of both modes are exclusively from the spin-wave components in the *ab* plane ($0.5S_{xx} + 0.5S_{yy}$). The spin gap originates from the rotation of the spins from the easy axis c to the *ab* plane, neglecting any "optical" magnons along c. This

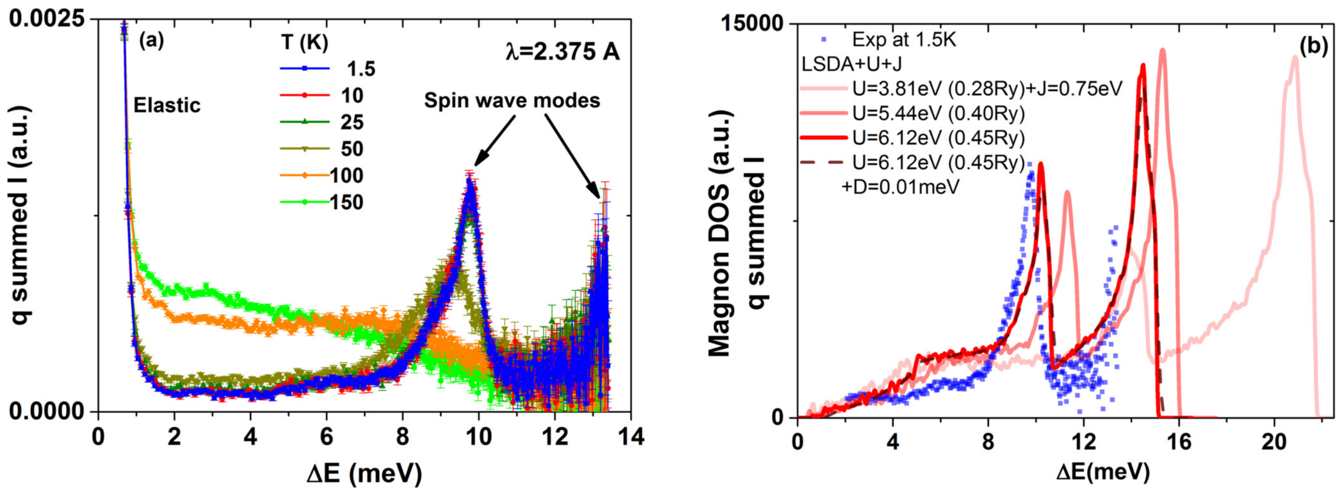

FIG. 10. (a) Energy-transfer dependence of the q summed intensity at various temperatures. (b) Comparison of the calculated magnon density of states (DOS) with the experimental q summed intensity at $T = 1.5$ K for various U and easy-axis anisotropy parameter D_{zz}.

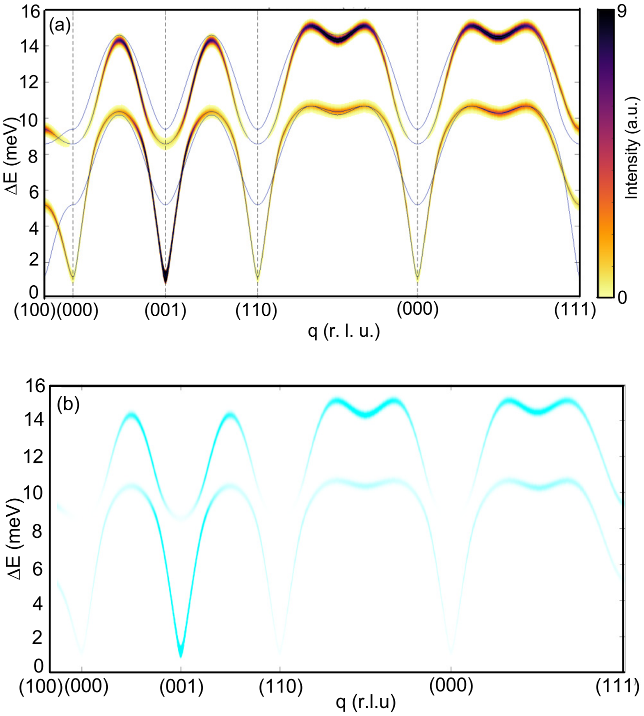

FIG. 11. (a) Simulated spin-wave spectra $[S_{\perp}(q,\omega)]$ along different directions and (b) out of easy-axis component $(0.5S_{xx} + 0.5S_{yy})$ of the simulated spin waves. Both of them are calculated from the exchange parameters J_i obtained for the LSDA + $U = 6.12$ eV (0.45 Ry) case. The dark blue curves on the top image correspond to the possible spin-wave modes in this system. The instrument resolution was selected to be 0.3 meV.

is in contrast to the similar compound $Co_4Nb_2O_9$, where the spins are aligned on the *ab* easy plane, and which has a gapless "Goldstone mode" for the excitations within the *ab* plane and a gapped mode out of the *ab* plane [21]. The pure gapped modes in $Mn_4Ta_2O_9$ further strengthen our statement that it behaves as a 3*d* Ising system and the role of the magnetic anisotropy enables multiple types of magnetic structures in this family of materials. This system is therefore comparable to the easy-axis system MnF_2, which also contains Mn^{2+} and the magnetic excitations are gapped [67]. We also calculated the magnon DOS which facilitates a direct comparison with the q summed intensity [Fig. 10(b)]. A good agreement of the calculated magnon DOS with experiment is achieved for the LSDA + $U = 6.12$ eV (0.45 Ry) case. As discussed above, a reduction of U results in a reduction of the band gap and an increase of the exchange, which will drive the spin modes to higher energies. Also, increasing the anisotropy from $D_{zz} = 0.01$ to 0.1 meV increases the spin gap to around 4 meV (see Fig. 8 in the Supplemental Material [39]), close to the value obtained from the heat-capacity measurements, but at the same time this will drive the modes to higher energies.

IV. SUMMARY

In summary, we investigated the role of spin interactions and spin (electron) correlation in determining the magnetic and possibly the multiferroic properties in $Mn_4Ta_2O_9$. For $Mn_4Ta_2O_9$, magnetic long-range order sets in at $T_N \sim 102$ K with strong exchange striction and small magnetic anisotropy. No structural phase transitions due to exchange striction were detected below T_N. The magnetic structure is described by a $k = (0,0,0)$ magnetic cell, consisting of ferromagnetic Mn^{2+} chains along c that are coupled antiferromagnetically with its neighbors through coplanar and a distorted honeycomb sublattice of Mn1 and Mn2, respectively. The magnetic moments of two crystallographically distinct Mn^{2+} ions are in the high-spin state with almost full spin moments for a $S = 5/2$ system. Critical exponents $\alpha = +0.17$ and $\beta = 0.34$ reveal the critical behavior of this magnetic system to be described by the three-dimensional Ising model, and thus explaining the easy-axis orientation of the moments obtained from NPD. Two gapped modes on the *ab* plane, originating from the tilting of the spins from the easy axis c were observed from INS experiments and confirmed by spin-wave simulations. The strongest exchange interactions J_i are within the Mn^{2+} honeycombs, which explains why the diffuse magnetic scattering is observed above T_N and associated with the two-dimensional spin correlations. The experimentally found high-spin state of Mn^{2+} is theoretically reproduced and the orbital occupation reveals the presence of only a very small orbital polarization and therefore a very weak SOC. The magnetic anisotropy and, consequently, the ground state of $Mn_4Ta_2O_9$ are determined by an electron-correlation-assisted magnetic dipole-dipole interaction. These results will facilitate the development of general magnetic model(s) with competing anisotropies influenced by the electron correlation, to provide a comprehensive understanding of the $M_4A_2O_9$ (M = Co, Fe, Mn, etc.) material family with different ground states.

ACKNOWLEDGMENTS

N. N. and Y. L. acknowledge the support of the Australian Research Council (ARC) in the form of Discovery Project (Project No. DP1601104780). N.N., Y.L., D.Y., and G.M. thank ANSTO for the allocation of neutron beam time on PELICAN (P6698) as well as financial support. N.N. and H.F. thank MLZ for the allocation of neutron beam time on SPODI (ID: 11618) and the HHLR Darmstadt for the allocation of computer time through Project No. 611.

[1] I. E. Dzyaloshinskii, J. Exp. Theor. Phys. **10**, 628 (1959).
[2] D. N. Astrov, J. Exp. Theor. Phys. **11**, 708 (1960).
[3] H. Schmid, Ferroelectrics **162**, 317 (1994).
[4] S.-W. Cheong and M. Mostovoy, Nat. Mater. **6**, 13 (2007).
[5] Y. Tokura and S. Seki, Adv. Mater. **22**, 1554 (2010).
[6] M. Kenzelmann, A. B. Harris, S. Jonas, C. Broholm, J. Schefer, S. B. Kim, C. L. Zhang, S.-W. Cheong, O. P. Vajk, and J. W. Lynn, Phys. Rev. Lett. **95**, 087206 (2005).

[7] O. Prokhnenko, R. Feyerherm, E. Dudzik, S. Landsgesell, N. Aliouane, L. C. Chapon, and D. N. Argyriou, Phys. Rev. Lett. **98**, 057206 (2007).

[8] N. Narayanan, P. J. Graham, N. Reynolds, F. Li, P. Rovillain, J. Hester, J. Kimpton, M. Yethiraj, G. J. McIntyre, W. D. Hutchison, and C. Ulrich, Phys. Rev. B **95**, 075154 (2017).

[9] G. Lawes, A. B. Harris, T. Kimura, N. Rogado, R. J. Cava, A. Aharony, O. Entin-Wohlman, T. Yildrim, M. Kenzelmann, C. Broholm, and A. P. Ramirez, Phys. Rev. Lett. **95**, 087205 (2005).

[10] I. Kornev, M. Bichurin, J.-P. Rivera, S. Gentil, H. Schmid, A. G. M. Jansen, and P. Wyder, Phys. Rev. B **62**, 12247 (2000).

[11] R. Toft-Petersen, M. Reehuis, T. B. S. Jensen, N. H. Andersen, J. Li, M. D. Le, M. Laver, C. Niedermayer, B. Klemke, K. Lefmann, and D. Vaknin, Phys. Rev. B **92**, 024404 (2015).

[12] Y. Fang, Y. Q. Song, W. P. Zhou, R. Zhao, R. J. Tang, H. Yang, L. Y. Lv, S. G. Yang, D. H. Wang, and Y. W. Du, Sci. Rep. **4**, 3860 (2014).

[13] Y. Fang, W. P. Zhou, S. M. Yan, R. Bai, Z. H. Qian, Q. Y. Xu, D. H. Wang, and Y. W. Du, J. App. Phys. **117**, 17B712 (2015).

[14] Y. Fang, S. M. Yan, L. Zhang, Z. Han, B. Qian, D. H. Wang, and Y. Du, J. Am. Ceram. Soc. **98**, 2005 (2015).

[15] N. D. Khanh, N. Abe, H. Sagayama, A. Nakao, T. Hanashima, R. Kiyanagi, Y. Tokunaga, and T. Arima, Phys. Rev. B **93**, 075117 (2016).

[16] H. Ehrenberg, G. Wltschek, H. Weitzel, F. Trouw, J. H. Buettner, T. Kroener, and H. Fuess, Phys. Rev. B **52**, 9595 (1995).

[17] E. F. Bertaut, L. Corliss, F. Forrat, R. Aleonard, and R. Pauthenet, J. Phys. Chem. Sol. **21**, 234 (1961).

[18] E. Fischer, G. Gorodetsky, and R. M. Hornreich, Solid State Commun. **10**, 1127 (1972).

[19] W. P. Osmond, Proc. Phys. Soc. **83**, 85 (1964).

[20] I. V. Solovyev and T. V. Kolodiazhnyi, Phys. Rev. B **94**, 094427 (2016).

[21] G. Deng, Y. Cao, W. Ren, S. Cao, A. J. Studer, N. Gauthier, M. Kenzelmann, G. Davidson, K. C. Rule, J. S. Gardner, P. Imperia, C. Ulrich, and G. J. McIntyre, Phys. Rev. B **97**, 085154 (2018).

[22] B. Schwarz, D. Kraft, R. Theissmann, and H. Ehrenberg, J. Magn. Magn. Mater. **322**, L1 (2010).

[23] M. Hoelzel, A. Senyshyn, and O. Dolotko, J. Large-scale Res. Fac. **1**, 5 (2015).

[24] T. Faske and W. Donner, J. Appl. Cryst. **51**, 761 (2018).

[25] H. M. Rietveld, J. Appl. Cryst. **2**, 65 (1969).

[26] J. Rodríguez-Carvajal, Physica B **192**, 55 (1993).

[27] D. H. Yu, R. A. Mole, T. Noakes, S. J. Kennedy, and R. A. Robinson, J. Phys. Soc. Japan **82**, SA027 (2013).

[28] D. Richard, M. Ferrand, and G. J. Kearley, J. Neutron Res. **4**, 33 (1996).

[29] S. Toth and B. Lake, J. Phys.: Condens. Matter **27**, 166002 (2015).

[30] http://elk.sourceforge.net/ (unpublished).

[31] K. H. Schwarz, P. Blaha, and G. K. H. Madsen, Comput. Phys. Commun. **147**, 71 (2002).

[32] J. P. Perdew and Y. Wang, Phys. Rev. B **45**, 13244 (1992).

[33] J. P. Perdew, K. Burke, and M. Ernzerhof, Phys. Rev. Lett. **77**, 3865 (1996).

[34] J. P. Perdew, A. Ruzsinszky, G. I. Csonka, O. A. Vydrov, G. E. Scuseria, L. A. Constantin, X. Zhou, and K. Burke, Phys. Rev. Lett. **100**, 136406 (2008).

[35] M. T. Czyżyk and G. A. Sawatzky, Phys. Rev. B **49**, 14211 (1994).

[36] V. I. Anisimov, J. Zaanen, and O. K. Andersen, Phys. Rev. B **44**, 943 (1991).

[37] O. Eriksson, M. S. S. Brooks, and B. Johansson, Phys. Rev. B **41**, 7311(R) (1990).

[38] F. Tran, P. Blaha, K. Schwarz, and P. Novák, Phys. Rev. B **74**, 155108 (2006).

[39] See Supplemental Material at http://link.aps.org/supplemental/10.1103/PhysRevB.98.134438 for additional information regarding SE: Experimental and calculation details; SB: Magnetic structure; SC: Exchange striction; SD: Electronic structure; SE: Heat capacity; and SF: Inelastic neutron scattering.

[40] M. Rotter, M. Loewenhaupt, M. Doerr, A. Lindbaum, H. Sassik, K. Ziebeck, and B. Beuneu, Phys. Rev. B **68**, 144418 (2003).

[41] E. Granado, J. W. Lynn, R. F. Jardim, and M. S. Torikachvili, Phys. Rev. Lett. **110**, 017202 (2013).

[42] E. F. Bertaut, J. Phys. Colloques **32**, C1-462 (1971).

[43] E. F. Bertaut, J. Appl. Phys. Suppl. **33**, 1138 (1962).

[44] Y. A. Izyumov, J. Magn. Magn. Mater. **15-18**, 497 (1980).

[45] F. Kagawa, K. Miyagawa, and K. Kanoda, Nature (London) **436**, 534 (2005).

[46] A. V. Andreev, M. I. Bartashevich, A. V. Deryagin, S. M. Zadvorkin, and E. N. Tarasov, ZhETF **94**, 218 (1988) [J. Exp. Theor. Phys. **67**, 771 (1988)].

[47] L. Vocadlo, K. S. Knight, G. D. Price, and I. G. Wood, Phys. Chem. Minerals **29**, 132 (2002).

[48] S. A. Hayward, S. A. T. Redfern, and E. K. H. Salje, J. Phys: Condens. Mater **14**, 10131 (2002).

[49] I. V. Solovyev, P. H. Dederichs, and V. I. Anisimov, Phys. Rev. B **50**, 16861 (1994).

[50] E. R. Ylvisaker, W. E. Pickett, and K. Koepernik, Phys. Rev. B **79**, 035103 (2009).

[51] N. S. Fedorova, C. Ederer, N. A. Spaldin, and A. Scaramucci, Phys. Rev. B **91**, 165122 (2015).

[52] H. J. Xiang, E. J. Kan, Su-Huai Wei, M.-H. Whangbo, and X. G. Gong, Phys. Rev. B **84**, 224429 (2011).

[53] R. Logemann, A. N. Rudenko, M. I. Katsnelson, and A. Kirilyuk, J. Phys: Condens. Mater **29**, 335801 (2017).

[54] G. Fischer, M. Däne, A. Ernst, P. Bruno, M. Lüders, Z. Szotek, W. Temmerman, and W. Hergert, Phys. Rev. B **80**, 014408 (2009).

[55] X. Wan, Q. Yin, and S. Y. Savrasov, Phys. Rev. Lett. **97**, 266403 (2006).

[56] J.-X. Zhu, M. Janoschek, R. Rosenberg, F. Ronning, J. D. Thompson, M. A. Torrez, E. D. Bauer, and C. D. Batista, Phys. Rev. X **4**, 021027 (2014).

[57] K. Rickert, E. A. Pozzi, R. Khanal, M. Onoue, G. Trimarchi, J. E. Medvedeva, M. C. Hersam, R. P. Van Duyne, and K. R. Poeppelmeier, Inorg. Chem. **54**, 6513 (2015).

[58] S. Kobayashi, Y. Nohara, S. Yamamoto, and T. Fujiwara, Phys. Rev. B **78**, 155112 (2008).

[59] S. Biermann, J. Phys.: Condens. Matter **26**, 173202 (2014).

[60] J. M. Tomczak, P. Liu, A. Toschi, G. Kresse, and K. Held, Eur. Phys. J. Special Topics **226**, 2565 (2017).

[61] H.-J. Koo, H. Xiang, C. Lee, and M.-H. Whangbo, Inorg. Chem. **48**, 9051 (2009).

[62] H.-J. Koo and M.-H. Whangbo, Inorg. Chem. **53**, 3812 (2014).

[63] D. C. Johnston, Phys. Rev. B **93**, 014421 (2016).

[64] R. Nath, K. M. Ranjith, B. Roy, D. C. Johnston, Y. Furukawa, and A. A. Tsirlin, Phys. Rev. B **90**, 024431 (2014).

[65] D. C. Johnston, R. J. McQueeney, B. Lake, A. Honecker, M. E. Zhitomirsky, R. Nath, Y. Furukawa, V. P. Antropov, and Y. Singh, Phys. Rev. B **84**, 094445 (2011).

[66] J. C. Lashley, R. Stevens, M. K. Crawford, J. Boerio-Goates, B. F. Woodfield, Y. Qiu, J. W. Lynn, P. A. Goddard, and R. A. Fisher, Phys. Rev. B **78**, 104406 (2008).

[67] O. Nikotin, P. A. Lindgard, and O. W. Dietrich, J. Phys. C **2**, 1168 (1969).